Chemical disorder and ^{207}Pb hyperfine fields in the magnetoelectric multiferroic $Pb(Fe_{1/2}Sb_{1/2})O_3$ and its solid solution with $Pb(Fe_{1/2}Nb_{1/2})O_3$

Yu. O. Zagorodniy,[1,2] R. O. Kuzian,[2,3] I. V. Kondakova,[2] M. Maryško,[4] V. Chlan,[1] H. Štěpánková,[1] N. M. Olekhnovich,[5] A. V. Pushkarev,[5] Yu. V. Radyush,[5] I. P. Raevski,[6] B. Zalar,[7] V. V. Laguta,[4,8] and V. A. Stephanovich[8]

[1]*Charles University, Faculty of Mathematics and Physics, V Holešovičkach 2, 180 00 Prague 8, Czech Republic*
[2]*Institute for Problems of Materials Science NAS Ukraine, Krjijanovsky 3, 03142 Kyiv, Ukraine*
[3]*Donostia International Physics Center (DIPC), ES-20018 Donostia-San Sebastian, Spain*
[4]*Institute of Physics AS CR, Cukrovarnicka 10, 162 00 Prague 6, Czech Republic*
[5]*Scientific-Practical Materials Research Centre, NAS Belarus, P.Brovki 19, 220072 Minsk, Belarus*
[6]*Physics Research Institute and Faculty of Physics, Southern Federal University, Rostov-on-Don, 344090, Russia*
[7]*J. Stefan Institute and J. Stefan International Postgraduate School, Ljubljana, Slovenia*
[8]*Institute of Physics, Opole University, Oleska 48, 45–052, Opole, Poland*

(Received 11 April 2017; revised manuscript received 26 September 2017; published 10 January 2018)

We report on the results of magnetic susceptibility, electron paramagnetic resonance, and ^{207}Pb nuclear magnetic resonance (NMR) studies of the magnetoelectric multiferroic $Pb(Fe_{1/2}Sb_{1/2})O_3$ (PFS) ceramic, as well as its solid solution with $Pb(Fe_{1/2}Nb_{1/2})O_3$ (PFN) of different degrees of the 1:1 ordering of magnetic Fe^{3+} and nonmagnetic Sb^{5+} ions. The ordering has been studied by x-ray diffraction (XRD) and NMR methods. In particular, two spectral lines, originating from the ordered and disordered regions, respectively, are resolved in the ^{207}Pb NMR spectra. This demonstrates the presence of spatially heterogeneous ordering where ordered regions are embedded into a disordered matrix. Combining XRD and NMR data, we have determined both the long-range order parameter s and the volume fraction of ordered regions s' for all investigated samples. The values vary in the range $s = 0-0.93$ and $s' = 0-1$. We have found that the ^{207}Pb Fermi contact interaction strongly depends on the disorder in the Fe/Sb positions: whereas it reaches 7.08 MHz in the ordered lattice, it is almost zero in the disordered environment. These results are further supported by the studies of PFS-PFN solid solutions. The analysis of experimental data in terms of density functional theory reveals a noticeably higher hybridization between Pb 6s and Fe 3d orbitals in the ordered case. The ordering of magnetic and nonmagnetic ions has a strong impact on the magnetic properties of PFS, leading to a transformation of the long-range ordered antiferromagnetic phase in chemically ordered samples to the spin glass state already in partially ($s = 0.35$) disordered specimens. In our opinion, the difference in the magnetic properties of PFN and PFS is related to the fact that PFN is completely disordered, in contrast to PFS, which is only partially disordered, with small ordered regions existing in the disordered matrix that prevent the percolation of the nearest-neighbor Fe−Fe exchange interaction across the lattice.

DOI: 10.1103/PhysRevMaterials.2.014401

I. INTRODUCTION

Multiferroics are materials with two or more types of spontaneous ordering (for instance, magnetic, electric, or elastic) coexisting in the same phase. Among them, magnetoelectric (ME) materials, which exhibit the coupling of electric polarization and magnetization at room temperatures, are very promising for spintronics and magnetic random access memory applications [1,2]. Until recently, the only known single-phase room-temperature multiferroic, suitable for such applications, was $BiFeO_3$ [3] and much attention has been paid to the quest for new single-phase multiferroic materials with the magnetoelectric phase at room temperature. Giant ME effect has been observed in a hexaferrite $Ba_{0.52}Sr_{2.48}Co_2Fe_{24}O_{41}$ single crystal (ME coupling ~3000 ps/m) [4]. It has also been discovered that room-temperature values of the ME coefficient of highly resistive $Pb(Fe_{1/2}Nb_{1/2})O_3$ (PFN) ceramics exhibit an order of magnitude larger values than those found in $BiFeO_3$ [5,6]. In the antiferromagnetic (AFM) phase of PFN (below 150 K), this difference is up to three orders of magnitude [6] and is assumed to be related to the averaging of the ME coupling in $BiFeO_3$ by spin rotations along the spin cycloid. Some success has also been achieved for perovskite solid solutions $Pb(Zr,Ti)O_3 - Pb(Fe_{1/2}Ta(Nb)_{1/2})O_3$ [7–10], $Pb(Fe_{2/3}W_{1/3})O_3-PbTiO_3$ [11], and $BiFeO_3-BiScO_3$ [12]. It has been also reported that $Pb(Fe_{1/2}Sb_{1/2})O_3$ (PFS) ceramics exhibit unexpectedly strong magnetic relaxor properties along with ferroelectricity reaching up close to room temperatures [13]. Studies of $Pb(Fe_{1/2}M_{1/2})O_3$ multiferroics have attracted particular attention in view of their double perovskite character (M = Nb, Ta, Sb).

All the above mentioned compounds belong to the family of B-cation disordered materials, where both the magnetic Fe^{3+} and the nonmagnetic M^{5+} ions can be either chemically ordered or randomly distributed over octahedral sites of the $A(B'B'')O_3$ perovskite structure (Fig. 1). The degree of chemical ordering depends strongly on the ionic radii of the Fe^{3+} and M^{5+} cations. It is commonly accepted that both $Pb(Fe_{1/2}Nb_{1/2})O_3$ and $Pb(Fe_{1/2}Ta_{1/2})O_3$ (PFT) are chemically disordered compounds due to almost matching ionic radii of

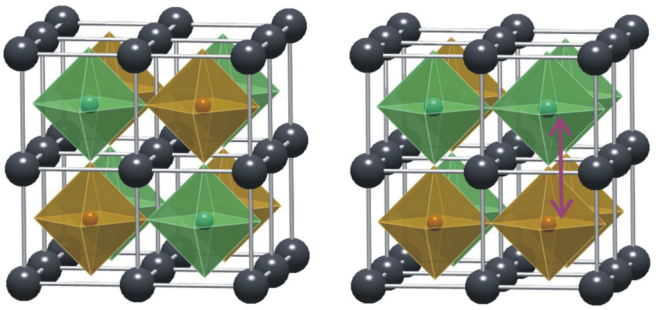

FIG. 1. A fragment of $A(Fe_{1/2}M_{1/2})O_3$ crystal structure containing $2 \times 2 \times 2$ perovskite cells. Black circles denote nonmagnetic A = Pb, Ca, Sr, Ba ions; green (brown) circles inside oxygen octahedra depict M (Fe) ions. Oxygen ions are located at the octahedral corners. Left panel shows the distribution of Fe and M ions in the chemically ordered structure. Disordered structure can be obtained, for instance, by swapping a pair of ions as indicated in the right panel.

Fe^{3+} and Nb^{5+} or Ta^{5+}, while Sb-containing compounds can be chemically ordered up to 90%–95% as Sb^{5+} is much larger than Fe^{3+} [14]. To model the order/disorder effects and magnetic interactions in these materials, six PFB0 … PFB5 periodic lattices with the supercells containing $2 \times 2 \times 2$ perovskite cells of different configurations of local chemical order (Fe/M ion distribution) had been considered in Refs. [15,16] (Fig. 2).

The magnetic properties of double perovskites are determined by Fe^{3+} (electron spin $S = 5/2$) ions, which occupy half of the octahedral sites of the perovskite structure (Fig. 1) and interact via various superexchange paths (Fig. 2). The largest superexchange energy $J_1/k_B \sim 50-70$ K results from the nearest-neighbor Fe−Fe interaction (Fe ions separated by the edge of the perovskite unit cell and interacting via the shortest Fe−O−Fe path) and from the next-nearest-neighbor interaction $J_2 \ll J_1$ (Fe ions separated by the face diagonal of the cell) [13,16].

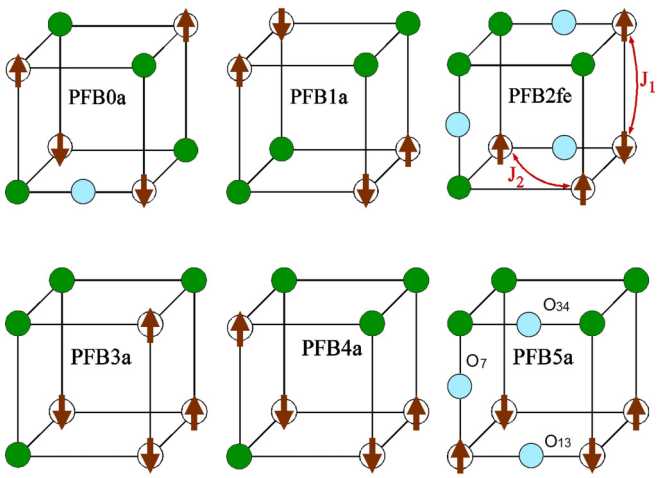

FIG. 2. Magnetic ground states for different chemical configurations of Fe^{3+} (arrows in open circles) in a $2 \times 2 \times 2$ supercell of $PbFe_{1/2}M_{1/2}O_3$ (only B-sublattice sites are shown). Green and light blue filled circles denote nonmagnetic M^{5+} and nonequivalent oxygen ions, respectively. J_1 and J_2 is the nearest- and next-nearest-neighbor Fe-Fe exchange interaction, respectively. Ferrimagnetic and antiferromagnetic ground states for different chemical configurations of Fe^{3+} ions are denoted as PFB2fe and PFB1a, PFB3a, and PFB4a, respectively (for details see Refs. [15,16]).

The variety of magnetic properties in various double perovskite compounds is commonly assumed to be the consequence of chemical ordering diversity [13,16–18]. However, this conjecture has never been confirmed experimentally, since different ordering degrees were always due to the differences in the nature of the M cations. Similarly, rather large (50–70 K) changes in the Neel temperature T_N of PFN and PFT, controlled by Li doping [19], mechanoactivation [20], and/or misfit strains in epitaxial films [21], were ascribed to the variations in the B-site cation ordering. Since no superstructural lines corresponding to long-range ordering were concurrently observed by x-ray diffraction, such ordering can only take place at the nanoscale.

In this paper, we report on the synthesis of PFS ceramics with different degrees of chemical ordering of the Fe^{3+} and Sb^{5+} ions. We also report on the studies of the impact of chemical ordering on the magnetic properties and on the local structural ordering of PFS, monitored by ^{207}Pb nuclear magnetic resonance (NMR) and Fe^{3+} electron paramagnetic resonance (EPR) measurements. This material is of considerable interest as it can be synthesized in a highly chemically ordered state [13,14] and possesses both magnetic and ferroelectric ordering [13]. It has a cubic paraelectric phase (space group $Fm\bar{3}m$), which transforms below $T \approx 190$ K into a polar phase with currently unknown symmetry [13,14]. An antiferromagnetic phase transition takes place in the chemically ordered sample at $T_N = 32$ K. In addition, PFS exhibits unexpectedly strong high-temperature magnetic relaxor properties due to formation of giant superspins below $T \approx 250$ K, which subsequently freeze-out into a superspin glass phase below $T_g \approx 140$ K [13].

The interplay between chemical order and/or disorder is further studied in the xPFS − (1-x)PFN solid solutions. In particular, we show that Nb ions play a major role in establishing chemical disorder in these solid solutions. We as well report on the calculations of electronic structure for different cation distributions in a periodic lattice of supercells, performed in order to apprehend the relationship between the hyperfine field of the ^{207}Pb nucleus and the disorder of the Fe/Sb sublattice.

Let us note that similar PFS samples with different degrees of ordering have previously been characterized by dielectric spectroscopy [13,22]. Surprisingly, the broadening of the dielectric permittivity maximum for the samples with very different degrees of chemical ordering ($s' = 0.46-0.9$) appeared to be almost the same and the temperature of this maximum did not depend on frequency. This result is rather unexpected, since in other $PbB^{3+}_{1/2}M^{5+}_{1/2}O_3$ (B^{3+}: Sc, In, Yb; M^{5+}: Nb, Ta) perovskites, cation disordering leads to a dramatic broadening of the permittivity maximum and a relaxorlike dielectric behavior [23–27].

II. EXPERIMENTAL

PFS and xPFS − (1-x)PFN solid solution ceramic samples were prepared in two stages. First, we synthesized the stoichiometric composition of PFS and xPFS − (1-x)PFN from the initial PbO, Fe_2O_3, Nb_2O_5, and S_2O_5 oxides at 1020–1030 K

for 4 hours. The resulting compounds were composed of different crystalline phases such as pyrochlore, perovskite, and some other. At $x > 0.6$, the prevalent phase is that with the oxygen-deficient $A_2B_2O_6$ pyrochlore structure, while the perovskite phase dominates at $x < 0.3$. To obtain PFS ceramics with perovskite structure and different degree of Fe^{3+} and Sb^{5+} ordering, a second stage of the synthesis has been performed at a hydrostatic pressure of 6 GPa, with temperatures varying from 1200 to 1800 K for PFS and from 1400 to 1800 K for xPFS − (1-x)PFN solid solution. The product of this approach, with the second-step synthesis duration times ranging from 0.3 to 10 min, is a dense coarse-grained (grain size 1−5 μm with a mean of ≈2 μm) ceramic of PFS and xPFS − (1-x)PFN, with an almost perfect perovskite structure void of any detectable parasitic phases. The room-temperature x-ray diffraction (XRD) patterns of both PFS and xPFS − (1-x)PFN samples correspond to cubic symmetry (space group $Fm\bar{3}m$) and exhibit superstructure lines. These are attributed to the presence of double perovskite unit cells associated with long-range chemical ordering of Fe^{3+} and Sb^{5+} ions [14].

Magnetic measurements were carried out in the 2–350 K temperature range using SQUID magnetometers MPMS-5S and MPMS-XL (Quantum Design) under field cooling (FC) and zero-field cooling (ZFC) protocols in the dc regime at fields of 100–70 000 Oe. Electron paramagnetic resonance measurements were performed at 9.407 GHz in the temperature range from 4 to 300 K, by employing the Bruker E580 spectrometer and Oxford Instrument cryostat.

Nuclear magnetic resonance measurements were performed using a commercial Bruker (Avance II) 400 MHz NMR spectrometer at 9.41 T (room-temperature measurements) and at 8.92 T (measurements at 77–450 K with the liquid N_2 Oxford Instrument cryostat). Extremely broad ^{207}Pb spectra (widths of several hundred kilohertz to several megahertz) were accumulated by a frequency-stepped method acquiring spin-echoes at evenly spaced transmitter frequency increments covering the full width of the spectrum. Individual echoes were Fourier transformed and then superimposed in the frequency domain. In order to increase the signal-to-noise ratio, the quadrupolar Carr-Purcell-Maiboom-Gill (QCPMG) pulse sequence [28] was employed. A four-phase "exorcycle" phase sequence (xx, xy, x-x, x-y) was used to form echoes with minimal distortions due to antiechoes, ill-refocused signals, and piezoresonances [29]. The length of the $\pi/2$ pulse was typically $t_{\pi/2} = 3$ μs, the spin-echo delay time τ was 10–25 μs and the repetition delay time was 5–10 ms. Up to 10 echo signals were accumulated in each QCPMG pulse cycle with 10 000–16 000 scans for each transmitter frequency in the frequency-stepped experiments. The spin-spin relaxation time T_2 has been determined by exponential fitting of the spin-echo intensity decay versus τ at various temperatures.

III. EXPERIMENTAL RESULTS

A. X-ray diffraction

In order to determine the chemical ordering degree of the synthesized PFS and xPFS − (1-x)PFN samples, we compare the intensity of 111 XRD superstructure line I_{111} to the fundamental reflection 200 (I_{200}). In the case of homogeneous ordering, the intensity ratio I_{111}/I_{200} is proportional to the square of the long-range order parameter s, defined as $s = 2p$-1 [23–25], where p is an occupation number of the Fe atoms at the 4b sites of the $Fm\bar{3}m$ space group. In overall, all investigated PFS samples are found to be structurally heterogeneous, with ordered or partially ordered regions embedded into a disordered matrix. This conclusion is drawn from combining the analysis of XRD linewidths (Table I) and the measurements of ^{207}Pb NMR spectra, characterized by two lines corresponding to the ordered and disordered regions, respectively (see Sec. III D). In such a heterogeneous case, only an effective order parameter s_{eff} can be determined from the XRD data, as the intensity of the 111 superstructure line also depends on the volume fraction of the ordered regions visible in XRD. The effective order parameter is calculated as [23,24]

$$s_{\text{eff}} = \sqrt{(I_{111}/I_{200})_{\text{exp}}/(I_{111}/I_{200})_{\text{calc},s=1}}, \quad (1)$$

where the intensity ratio $(I_{111}/I_{200})_{\text{calc},s=1}$ is calculated within the assumption of perfect ordering, $s = 1$. Order parameters s and s_{eff} are related via $s_{\text{eff}}^2 = s^2 s'$, where s' denotes the fractional volume of the ordered (or partly ordered) regions. The latter can be estimated from the NMR spectra, which resolve separated lines from ordered and disordered regions regardless of their size (see Sec. III D). Thus, by combining XRD and NMR data, the long-range order parameter can be determined even for heterogeneous ordering. However, in the present paper, we will primarily use the effective order parameter s_{eff} for the characterization of our samples.

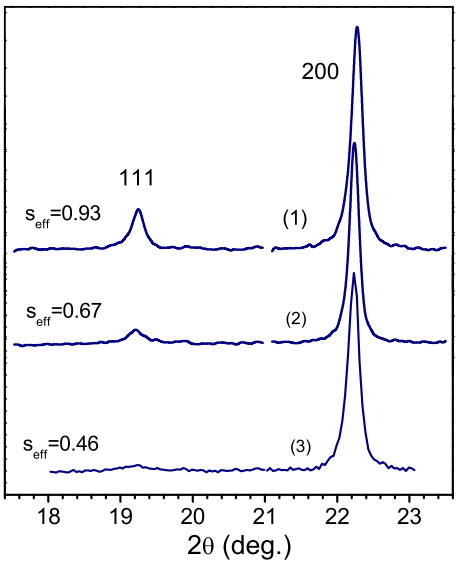

FIG. 3. Part of the x-ray diffraction pattern that shows the 111 superstructure and 200 main reflexes for the samples synthesized for 10 min at 1200 K [$s_{\text{eff}} = 0.93$, sample 1], 3 min at 1500 K ($s_{\text{eff}} = 0.67$, sample 2], and 0.3 min at 1700 K [$s_{\text{eff}} = 0.46$, sample 3].

Some typical x-ray diffraction patterns near the 111 and 200 peaks for PFS samples of different s_{eff} values are shown in Fig. 3, whereas Table I displays the order parameters and linewidths of all investigated specimens. As it can be discerned from Table I, the widths of the 111 and 200 reflexes nearly match in sample (1). This is not the case for other samples where the 111 superstructure linewidth is much larger than that

TABLE I. X-ray diffraction characterization of PFS samples with different chemical order and of xPFS − (1-x)PFN solid solution compositions. $s_{\rm eff}$ is the effective order parameter determined from the XRD data and s' the volume fraction of the ordered (or partly ordered) regions calculated from NMR spectra. $s = s_{\rm eff}\sqrt{s'}$ is the long-range order parameter. FWHM denotes the full width at-half maximum.

composition	sample No	$s_{\rm eff}$	(111), FWHM	(200), FWHM	s'	s
PFS	(1)	0.93	0.2^0	0.17^0	1	0.93
PFS	(2)	0.67	0.31^0	0.14^0	0.64	0.83
PFS	(3)	0.46	0.43^0	0.17^0	0.38	0.75
PFS	(4)	0.21	1.13^0	0.14^0	0.37	0.34
0.9PFS-0.1PFN	(5)	0.6			0.46	0.88
0.8PFS-0.2PFN	(6)	0.5			0.40	0.79
0.7PFS-0.3PFN	(7)	0.25			0.21	0.54
0.4PFS-0.6PFN	(8)	0			0.07	0
0.2PFS-0.8PFN	(9)	0			0	0

of the 200 reflexes. This indicates the formation of ordered regions with sizes much smaller than the size of ceramic grains. Table I values also imply that, at low PFS content ($x \leqslant 0.4$), xPFS − (1-x)PFN solid solutions do not exhibit the 111 superstructure XRD line arising from the double perovskite unit cell, despite the fact that sample preparation conditions were optimized to obtain the structure with the highest degree of chemical ordering.

B. Magnetic susceptibility data

Figures 4 and 5 report the magnetic susceptibilities, determined at two different magnetic fields, 500 Oe and 2 kOe, in PFS samples. The temperature behavior of the susceptibility of the samples with $s_{\rm eff} = 0.93$ and 0.67 at low fields of 300–500 Oe (Fig. 4) is similar to that reported previously [13]. On cooling, the susceptibility exhibits a gradual increase below 250 K, attributed to formation of superparamagnetic (SPM) clusters or superspins in disordered regions. On further cooling, a broad bump is observed between 100 and 150 K, ascribed to collective freezing of the SPM clusters into a superspin glass phase [13,30]. The bump is well visible at low fields, e.g., 300 Oe (the uppermost curve in Fig. 4), but is gradually suppressed on increasing the field. It disappears almost completely at a relatively low field of 2 kOe (Fig. 5, left panel). The formation of superspins from antiferromagnetically interacting Fe^{3+} spins is possible due to the existence of ferrimagnetic superstructures (see, e.g., PFB2fe configuration in Fig. 2). The response of the ferrimagnetic superstructures at low fields may substantially exceed the response of the ensemble of noninteracting spins [13,17]. However, at large enough fields, such superspins are saturated and do not contribute to the susceptibility.

The sharp maximum at $T = 32$ K in both FC and ZFC data corresponds to an AFM phase transition with the Neel temperature $T_N = 32$ K for a well-ordered sample ($s_{\rm eff} = 0.93$). One can also see that the anomalies, related to superspins, gradually disappear with decreasing chemical order. This is due to reduction in the cluster size of the superspin, resulting in conventional paramagnetic (PM) behavior. Simultaneously, the ZFC susceptibility peak shifts to $T \approx 20$ K and transforms into a cusp, characteristic of a transition into a classical spin glass state [31]. Moreover, below this temperature, ZFC and FC susceptibilities start to mismatch, indicating the onset of nonergodicity. The observed spin glass state is created by individual Fe^{3+} spins or small spin clusters. On the other hand, the superspin glass phase is formed by large spin clusters, embedded into paramagnetic matrix, with a total magnetic moment typically about 10 000 $\mu_{\rm B}$ [13].

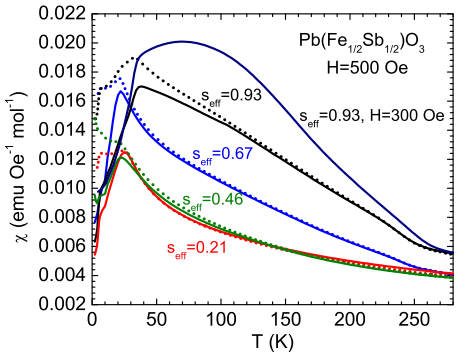

FIG. 4. Temperature dependence of the FC (dotted lines) and ZFC (solid lines) magnetic susceptibilities in the 500 Oe field for PFS samples with different chemical ordering degrees: $s_{\rm eff} = 0.93$, 0.67, 0.46, and 0.21. For the sample with $s_{\rm eff} = 0.93$, ZFC susceptibility in the 300 Oe field is shown as well.

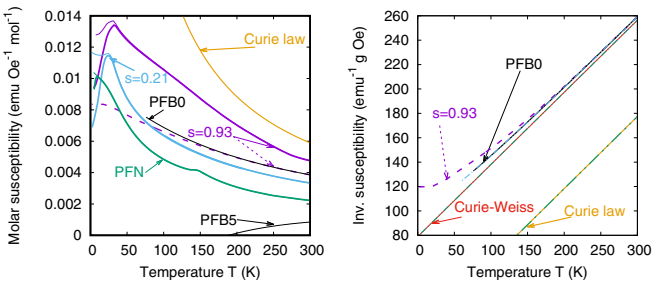

FIG. 5. (Left) Temperature dependence of the magnetic susceptibility of two PFS samples with the ordering degrees $s_{\rm eff} = 0.93$ and 0.21 at $H = 2$ kOe (magenta and cyan solid lines, respectively). Data for $s_{\rm eff} = 0.93$ at $H = 70$ kOe (magenta dash line) and for PFN ($s = 0$) are shown for comparison, along with the theoretical curves for PFB0 and PFB5 structures. (Right) Inverse susceptibility for the PFS sample with $s_{\rm eff} = 0.93$ at $H = 70$ kOe (magenta dash line) and its fit by the tenth-order high-temperature expansion of the PFB0 structure (see text below for explanation).

Another characteristic feature of our experimental results is the decrease of magnetic susceptibility with the increase of disorder in the system. In the following, we shall explain this behavior by considering the impact of exchange interaction among spins at different temperatures.

At high enough temperatures, $T > T_s \equiv J_{\max} S(S+1)$, with $J_{\max}$ denoting the strongest exchange interaction in the system, the magnetic susceptibility of the ensemble of interacting spins follows the Curie-Weiss law [32]:

$$\chi_{\rm CW} = [N(g\mu_B)^2 S(S+1)]/[3k_B(T-\theta)],$$

$$\theta = -\left[\frac{S(S+1)}{3k_B N}\sum_{\mathbf{R},\mathbf{r}(\mathbf{R})} J_{\mathbf{r}(\mathbf{R})}\right].$$

Here, μ_B is the Bohr magneton, g factor is assumed to be equal to 2.0023, $\mathbf{R}$ runs over all the spins, and $\mathbf{r}$ over all the bonds, equivalently over all spin pairs with exchange interaction $J_{\mathbf{r}(\mathbf{R})}$. For double perovskites, $N = N_A/2$, where N_A is the Avogadro number. The value of θ depends on the average exchange interaction of magnetic ions and is larger for disordered systems, for in this case some of the Fe^{3+} ions are separated by the shortest distance. Such pairs thus possess stronger superexchange energy $J_1 \gg J_2$ (see Fig. 2).

At $T < T_s$, the system's response depends not only on J_r but also on the spin arrangement geometry [17], one of PFB0 … PFB5 (Fig. 2). The left panel of Fig. 5 shows the calculated magnetic susceptibility of the PFB0 structure, which correspond to ordered PFS, and of the PFB5 layered structure, which models disordered samples. Theoretical susceptibility curves of Fig. 5 have been calculated using high-temperature series expansion (HTE) [17,33]. It is straightforward to see that $\chi(T)$ associated with PFB5, the configuration where each spin is coupled to four nearest neighbors by the strongest exchange $J_1/k_B \approx 70$ K, lies below all other curves at all temperatures.

In the PFB0 configuration, all spins are coupled only by the second-nearest neighbor exchange J_2 (Fig. 2). In order to determine the actual value of this coupling, we have fitted the experimental susceptibility $\chi(T) = M(T)/H$ ($H = 70$ kOe) of the sample with almost perfect ordering ($s_{\rm eff} = 0.93$) in the temperature interval 100 K $< T <$ 300 K by HTE expression (Fig. 5, right panel). We have taken into account that only fraction s' of the total number of spins contributes to the susceptibility. This is so since superspins from disordered regions with the relative volume 1-s' are saturated in high magnetic fields. The coefficients of HTE depend on the spin value. By calculating $\chi(T)$ with $S = 5/2$ and assuming that s' is solely responsible for the reduction of Curie constant, we obtain $J_2/k_B \approx 3.82$ K with unrealistically small $s' = 0.77$. Alternatively, using an effective spin value of $S = 2.20$, an approach justifiable for the scenario of covalence-induced spin reduction [34,35], we find $J_2/k_B \approx 4.73$ K with $s' \approx 0.96$ that well reproduces the experimentally observed value $s' \approx 1$ (Table I).

C. EPR data

By conjuring that disordered PFS samples only exhibit short-range spin ordering, we find EPR spectroscopy an appropriate method to monitor it. Usually, in magnetic materials with AFM spin coupling, EPR linewidth broadens critically on approaching the phase transition temperature. Such a behavior is a good indicator of spins' thermal motion freezing, regardless of their short- or long-range ordering. Moreover, the EPR spectrum disappears completely below the freezing temperature, as AFM-coupled spins have zero net magnetic moment and thus do not contribute to paramagnetic absorption.

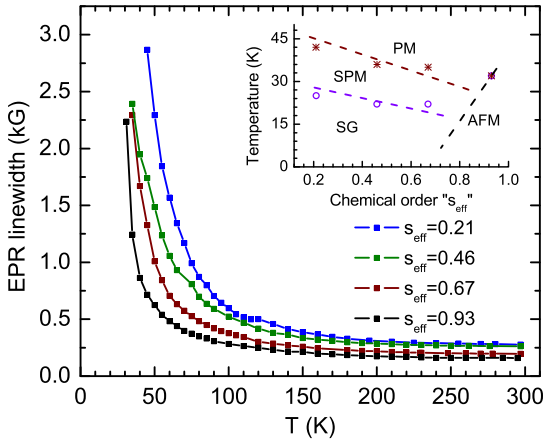

FIG. 6. Temperature dependence of Fe^{3+} EPR peak-to-peak linewidth for PFS samples with different chemical order $s_{\rm eff} = 0.21 - 0.93$. The inset shows a proposed T-s magnetic phase diagram of PFS. Dashed lines separate different magnetic phases: paramagnetic (PM), AFM, SPM, and spin-glass (SG) phases. Stars denote temperatures T^* at which the EPR absorption disappears, whereas circles denote temperatures of maximal magnetic susceptibilities.

Experimental temperature dependencies of EPR linewidths for all studied PFS samples are shown in Fig. 6. One can see that the EPR spectrum of the perfectly ordered sample ($s_{\rm eff} = 0.93$) broadens sharply on approaching the Neel temperature $T_{\rm N} =$ 32 K. An increase in chemical disorder results in a progressive spectral line broadening, as well as shifting of this broadening towards higher temperatures.

The temperature at which the EPR spectrum disappears coincides with that of the susceptibility maximum only for chemically ordered samples. For other samples, this temperature increases progressively with an increase in chemical disorder. Similar behavior was deduced from Mossbauer studies of PFS ceramics with different degrees of ordering [22]. Bearing in mind that EPR absorption indicates AFM spin ordering on the EPR time scale, we associate the temperature T^* of the disappearance of EPR spectra with the temperature of the emergence of small thermally reorienting AFM clusters. The respective state has been referred to as the superantiferromagnetic (SAFM) phase in Ref. [36]. On further cooling, this state develops into a spin (or cluster) glass state. The experimentally determined temperature-chemical order phase diagram, constructed by combining magnetic susceptibility and EPR data, is shown in the inset to Fig. 6. A PM phase exists at temperatures where PM absorption is present, i.e., Fe^{3+} ions behave as independent spins. With decreasing temperature, the PM phase transforms either into the AFM phase, in the samples with high chemical order, or into the SPM or SAFM phase, in the samples with low chemical order. On further temperature lowering, SPM/SAFM clusters freeze-out into a spin glass state of different types, such as the cluster glass [31,36] or superspin glass [13,30].

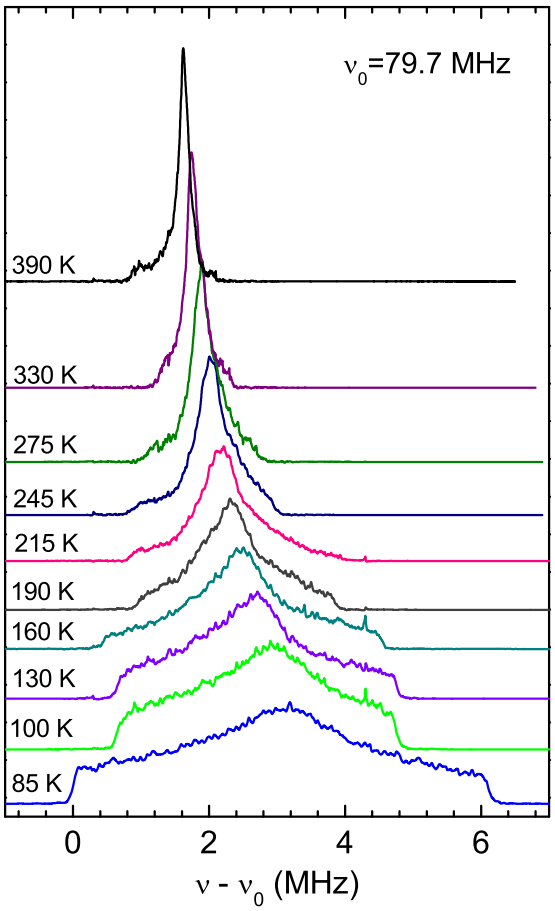

FIG. 7. ^{207}Pb NMR spectrum in PFS ($s_{\text{eff}} = 0.93$) at selected temperatures. Spectra are trimmed to the left and right at the intensity levels of about 10%−40% their maximum value.

D. ^{207}Pb NMR data

1. ^{207}Pb *hyperfine interaction*

We have investigated the local magnetic properties of PFS by performing ^{207}Pb NMR measurements. Corresponding spectra measured in the sample with almost perfect ordering ($s_{\text{eff}} = 0.93$) are shown in Fig. 7 for a selection of temperatures.

The spectrum is broad even at high temperatures and its linewidth strongly increases on temperature lowering. In order to keep the spectral accumulation at reasonable duration, acquisition was limited to a frequency interval within which individual frequency-stepped measurement points reached, in integrated intensity, at least 10% (high temperatures) to 40% (low temperatures) of the point of maximum intensity. As evident from Fig. 8, the spectrum shifts towards higher frequencies with decreasing temperature (about 3 MHz at 100 K). This behavior reveals the paramagnetic nature of PFS at the investigated temperatures. On the contrary, the ^{207}Pb NMR frequency shift of PFN (paramagnet at $T > 150$ K), also shown in Fig. 8, changes only slightly below the ferroelectric phase transition at $T_C \approx 370$ K [37].

The NMR frequency shift in PFS can be well described by the Fermi contact interaction mechanism [38]. Assuming that, in the chemically ordered regions (occupying up to 93% − 96% of the sample volume) the shift of the ^{207}Pb NMR is due

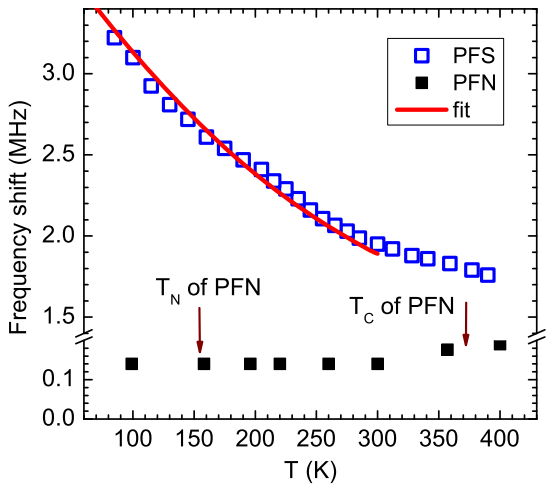

FIG. 8. Temperature dependence of ^{207}Pb NMR frequency shift for PFS, measured relative to the Larmor frequency 79.268 MHz of $Pb(NO_3)_2$. The ^{207}Pb NMR frequency shift for PFN is shown for comparison reasons. Solid line is the theoretical fit for the experimentally determined magnetic susceptibility in the magnetic field of $\mu_0 H = 7$ T flux density. Arrows mark the temperatures of the ferroelectric transition (T_C) and AFM transition (T_N) in PFN.

to the interaction with its four nearest-neighbor Fe^{3+} ions, the spin Hamiltonian reads

$$\mathbf{H} = -\gamma_N \hbar \mathbf{H}_0 \mathbf{I} + 4\mathbf{A}\mathbf{I}\langle S\rangle, \tag{1}$$

where $\mu_0 H_0 = 8.92$ T is the external magnetic field and $\gamma_N = 5.5767 \times 10^7$ rad s^{-1} T^{-1} is the gyromagnetic ratio of ^{207}Pb nuclei, $\langle S\rangle$ is the thermally averaged spin of Fe^{3+}, and A is the Fermi contact interaction constant (isotropic hyperfine constant). Spin $\langle S\rangle$ can be expressed in terms of molecular susceptibility χ_M as

$$\langle S\rangle = -\frac{\chi_M H_0}{N g \mu_B}, \tag{2}$$

where $N = N_A/2$, since only half of the octahedral sites are occupied by Fe^{3+} ions. For isotropic hyperfine interaction, the constant A can be calculated from the relation

$$h\Delta\nu = -4A\langle S\rangle, \tag{3}$$

where $\Delta\nu$ is the paramagnetic shift of the NMR line. Consequently,

$$A = -\frac{N_A g \mu_B h \Delta\nu}{8\chi_M H_0}. \tag{4}$$

The best fit of the ^{207}Pb NMR frequency shift for PFS is shown in Fig. 8 (red solid line). This fit has been obtained using the experimentally determined magnetic susceptibility at the field 70 kOe and $A = 7.08$ MHz. We note that the magnetic susceptibility saturates as a function of the magnetic field already at $H > 2000$ Oe [13]. Therefore the data at the field 70 kOe are valid at the field 90–94 kOe of NMR magnet as well. The agreement between measured and calculated frequency shifts is satisfactory, except in the temperature range above 300 K. This disparity can be explained in terms of temperature-dependent Fermi contact interaction, with the changes of the electron-nuclear interaction arising from the temperature

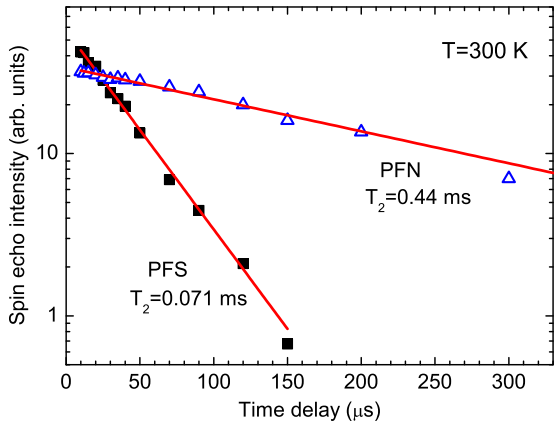

FIG. 9. ^{207}Pb spin-spin (T_2) relaxation measurements in PFS and PFN at 300 K.

variation of lattice parameters. X-ray diffraction measurements [14], indeed, detected a crystal structure transformation below 250–260 K. This agrees well with the aforementioned deviation of the theoretical curve from the experimental data at $T > 270$ K. Moreover, dielectric measurements support the existence of a ferroelectriclike phase transition at 190 K. Although the mismatch of theoretical and experimental data is not large, it nevertheless reflects a crystal structure transformation, associated with the phase transition.

2. NMR linewidth

The exchange interaction between electron spins leads to the narrowing of the ^{207}Pb NMR intrinsic (homogeneous) linewidth in the paramagnetic phase. Its value at $T = 300$ K, calculated in the conventional way as the reciprocal transverse relaxation time T_2, is 88.5 kHz ($T_2 = 0.071$ ms) for PFS and only 14.3 kHz ($T_2 = 0.44$ ms) for PFN (Fig. 9). Both values are much smaller than the total measured linewidth of ∼0.5−1 MHz. This proves that the spectrum is inhomogeneously broadened due to fluctuations of both electron-nucleus and exchange interactions from site to site.

The exchange-narrowed linewidth can be expressed as [39,40]

$$\frac{1}{T_2} = \frac{\sqrt{\pi/2}S(S+1)}{3\omega_e}\sum_{j,v}\left[\left(A^j_{zv}\right)^2 + \frac{1}{2}\left(A^j_{xv}\right)^2 + \frac{1}{2}\left(A^j_{yv}\right)^2\right], \tag{5}$$

where $v = x,y,z$, $A_{vv'}$ are the components of the electron-nucleus interaction tensor. The index j is running from 1 to 4 and accounts for the number of nearest-neighbor Fe^{3+} ions. The exchange frequency ω_e is defined as [40]

$$\hbar^2\omega_e^2 = \frac{2}{3}S(S+1)\sum_{j'}J^2_{jj'}. \tag{6}$$

Here, $J_{jj'}$ are the exchange integrals ($H_e = \sum_{j<j'} J_{jj'}S^jS^{j'}$). In the PFS ordered structure, each Fe^{3+} electron spin interacts with 12 nearest-neighbor spins with the strength $J_2 \approx 4.73$ K (determined above from the HTE fit of the magnetic susceptibility). This leads to the exchange frequency $\omega_e \approx 6 \times 10^{12}$ rad s^{-1} and the average A_v values

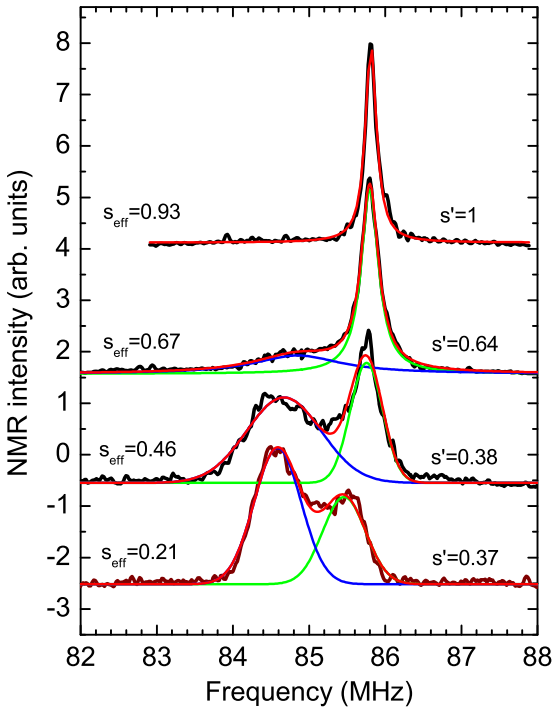

FIG. 10. Room-temperature ^{207}Pb NMR spectra (black lines) for PFS samples with different degrees of chemical order quantified by s_{eff} (as determined by x-ray diffraction, see Table I). Green and blue solid lines are spectral components (Gaussian fits) corresponding to chemically ordered and disordered regions, respectively. The relative occurrence of ordered regions, s', is calculated as the ratio between the partial spectral area associated with ordered regions (green lines), the total spectral area (red lines).

of about 8.6 MHz, a plausible result when taking into account that the isotropic part of the electron-nucleus interaction (Fermi contact interaction) is 7.08 MHz. In contrast to PFS, in PFN, the isotropic electron-nucleus interaction $A = \frac{1}{3}(A_{xx} + A_{yy} + A_{zz})$ is negligibly small as compared to A_{vv} components as no observable temperature shift of ^{207}Pb frequency has been detected (Fig. 8), apart from the weak decrease below the ferroelectric phase transition at ∼370 K. Nuclear relaxation in PFN is also much slower as compared to PFS due to a larger exchange frequency, which is now mainly determined by $J_1 \approx 70$ K [16].

3. Influence of the chemical disorder on NMR spectra

In order to check on the interplay between chemical disorder and electron-nuclear interaction, PFS samples with different degree of chemical order were investigated. ^{207}Pb NMR spectra for these samples are shown in Fig. 10.

One can see that, as the degree of disorder increases, the second spectral component appears at the frequency of 84.5 MHz. Its intensity increases with the decrease of effective order parameter s_{eff}. We attribute this low-frequency line to the resonance originating from chemically disordered regions of PFS samples. The relative volume of the chemically ordered regions, i.e., the order parameter s', is thus calculated as $s' = I_{\text{ord}}/(I_{\text{ord}} + I_{\text{disord}})$. Here I_{ord} and I_{disord} denote integrated spectral intensities of the peaks associated with ordered regions

(green spectral component of Fig. 10) and disordered regions (blue spectral component of Fig. 10), respectively. The experimental s' values are listed in Fig. 10 and Table I.

One can see that both order parameters, s_{eff} and s', determined by x-ray diffraction and by NMR, respectively, coincide rather well in the well-ordered samples ($s_{\text{eff}} = 0.93$ and 0.67), but deviate markedly from each other on diminishing the degree of order. In the sample with the weakest order ($s_{\text{eff}} = 0.21$, bottom spectrum of Fig. 10), the spectral component at 85.8 MHz belonging to ordered regions is two times broader than in the case of ordered sample (top spectrum of Fig. 10), as well as shifted towards lower frequencies. Nevertheless, this component can be clearly identified, with substantial integral intensity, even in most disordered samples. This demonstrates that local order, at the nanometric scale, still exists in the regions which are disordered at a larger scale (as evident from x-ray diffraction). Such persisting local chemical order, in our specific case the order of Fe and Sb ions, can suppress the tendency of increasing Neel temperature anticipated for disordered samples.

In general, our experimental data suggest that ^{207}Pb chemical shift, and thus the hyperfine field in PFS, essentially depends on chemical ordering. The hyperfine field is smaller in disordered regions than in ordered regions of PFS. In the paramagnetic phase, its value $4A\langle S\rangle$ depends on the hyperfine constant and on the magnetic susceptibility [see Eqs. (1) and (2)]. Both factors are smaller in disordered regions.

As the temperature dependence of ^{207}Pb NMR spectrum has not been measured in disordered PFS, the value of the Fermi contact interaction constant in the disordered regions of PFS can be estimated only roughly at 2.9 MHz, by using room-temperature magnetic susceptibility data and NMR line shifts measured relative to the NMR frequency of PFN. In PFN, the ^{207}Pb NMR frequency is almost temperature-independent at $T < 370$ K, even at the PM-AFM phase transition at $T_{\text{N}} \approx 150$ K (Fig. 8). Therefore we approximate the Fermi contact interaction constant in PFN as zero.

Let us emphasize that NMR can resolve spectral lines originating from both ordered and disordered regions, whereas x-ray diffraction resolves only superstructure lines arising from ordered regions within all reflections of the perovskite structure.

4. Chemical disorder and ^{207}Pb NMR spectra in the xPFS − (1-x)PFN solid solution

With the purpose of throwing some additional light on the origin of the two components in the ^{207}Pb NMR spectrum of PFS, we have performed measurements on the xPFS − (1-x)PFN solid solution. As PFN is believed to be a completely chemically disordered compound [41,42], substitution of Nb for Sb is anticipated to result in the diminishing of chemical order. Room-temperature NMR spectra of some xPFS − (1-x)PFN compositions are reported in Fig. 11. Similar to disordered PFS, these spectra are composed of two superimposed peaks (simulation with green and blue solid lines in Fig. 11). One of the resonance peaks (at 85.8 MHz, same frequency as in the ordered PFS) corresponds to regions where Pb nuclei are surrounded only by Sb and Fe ions with 1:1 order. The intensity of this peak decreases with increase

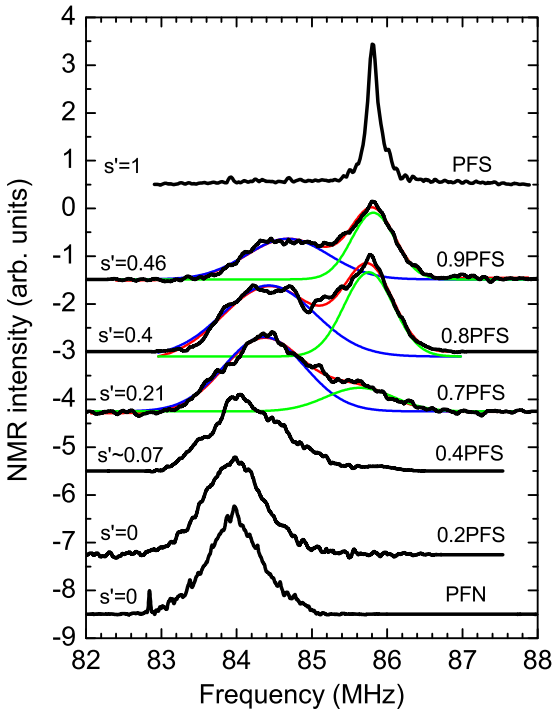

FIG. 11. ^{207}Pb NMR spectra of xPFS − (1-x)PFN compositions at room temperature. Black and red lines correspond to measured and simulated spectra, respectively. Green and blue solid lines are spectral components (Gaussian fits) corresponding to chemically ordered and disordered regions, respectively. The experimentally determined values of parameter s' are also shown.

of PFN share in the solid solution. Concurrently, its width progressively increases. On the contrary, the intensity of the second peak, near the frequency of 84.5 MHz, increases as the PFN share increases. Its resonance frequency exactly matches the one found for ^{207}Pb nuclei in the disordered regions of PFS.

Note that the volume fraction of chemically disordered regions in the xPFS − (1-x)PFN solid solution substantially increases even for small PFN concentration. Specifically, 50% of the sample volume is found to be in the disordered state in a solid solution that only contains 10% of PFN. These data reveal that chemical disorder is solely responsible for the rise of the second component in the ^{207}Pb spectrum, rather than chemical shift due to the presence of Nb ions.

In the 0.4PFS–0.6PFN solid solution, the peak related to chemically ordered regions almost disappears, and the position of the low-frequency peak moves towards the resonance frequency of PFN. X-ray diffraction patterns also exhibit vanishing 111 superstructure reflexes already at $x < 0.6$ (Table I), in support of chemically disordered state scenario of these compositions.

IV. DFT CALCULATIONS

A. ^{207}Pb Fermi contact interaction

To discern the possible origin of the anomalously strong Fermi contact interaction in the chemically ordered PFS structure and its substantial reduction in the disordered PFS structure, we performed density functional theory calculations

TABLE II. Results of the population analysis of Pb 6*s* orbitals for various chemical ordering and spin configurations with total spin of the supercell $2S_{\mathrm{Fe}} = 5$. The calculated population (total number of electrons per orbital) $n_{\mathrm{Pb6}s} = n_{\mathrm{Pb6}s,\uparrow} + n_{\mathrm{Pb6}s,\downarrow}$ and the magnetic moment $m_{\mathrm{Pb6}s} = n_{\mathrm{Pb6}s,\uparrow} - n_{\mathrm{Pb6}s,\downarrow}$ are shown in rows two and three, respectively.

Configuration	$n_{\mathrm{Pb6}s}$	$m_{\mathrm{Pb6}s}$
PFB0	1.90286	0.00182
PFB2	1.89892	0.00137
PFB5	1.89799	0.00077

within the atomic limit LSDA + U scheme [43,44] using the full-potential local-orbital (FPLO) code [45], as described in detail in Ref. [16]. We studied a cubic perovskite structure corresponding to PFS in the paraelectric phase with an experimental lattice parameter $a = 3.9468$ Å [14]. Here, we present data for the on-site repulsion parameter $U = 6$ eV and ferrimagnetic spin configuration with supercell total spin $2S_{\mathrm{Fe}} = 5$.

We assume that PFS stoichiometry is preserved on a short-range scale, and we adopt the model of disorder proposed in Ref. [15]. Specifically, we consider a periodic lattice with a supercell containing several perovskite cells with various chemical order (ion distributions) configurations. In the case where the supercell contains 40 atoms ($2 \times 2 \times 2$, $Pb_8Fe_4Sb_4O_{24}$), six configurations PFB0…PFB5 (for detail see Figs. 2 and 3 of Ref. [15] as well as Fig. 2 of Ref. [16]) are possible in the double perovskites. In this model, every Pb ion is surrounded by four nearest Fe ions, located at the vertices of a cube centered at the Pb ion. The arrangement of Fe ions is different for different configurations. Configurations PFB0, PFB2, and PFB5 are most energetically favorable in PFS [13,15]. In the ordered configuration PFB0, with Fe and Sb ions intermixed in the B sublattice of the perovskite structure, Fe ions occupy the vertices of a regular tetrahedron centered at Pb ion. In the layered PFB5 configuration, Fe ions form a square and occupy the vertices that belong to a face of the cube. In the PFB2 configuration, Fe ions occupy two nonequivalent positions and form a pyramid.

Magnetic moment of Fe^{3+} ion couples with the ^{207}Pb nuclear moment via a superhyperfine interaction. The main contribution to the hyperfine field at the Pb site comes from the Fermi contact interaction, which is proportional to the spin polarization of the electron density at the site of the nucleus,

$$H_c = \frac{8\pi}{3} g\beta g_n \beta_n \mathbf{I} \cdot \mathbf{S}\delta(\mathbf{r} - \mathbf{R}_{Pb}), \tag{7}$$

where g_n, β_n are the nuclear g factor and magneton, respectively. $\boldsymbol{S}$ is the Fe^{3+} spin. The integration over the electron orbital degrees of freedom yields $H_c = g_n \beta_n \mathbf{I} \cdot \mathbf{H}_{hf}$, with an effective hyperfine field

$$\mathbf{H}_{\mathrm{hf}} = -\frac{8\pi}{3} g\beta [n_\uparrow(\mathbf{R}_{\mathrm{Pb}}) - n_\downarrow(\mathbf{R}_{\mathrm{Pb}})]. \tag{8}$$

Here, $n_{\uparrow,\downarrow}(\mathbf{R}_{\mathrm{Pb}})$ denote the electron spin densities at the Pb nucleus. The main contribution to the polarization originates from Pb 6*s* valence orbitals. Table II shows that the spin moment of Pb 6*s* orbital, $m_{\mathrm{Pb6}s}$, strongly depends on the chemical order. The ideal tetrahedral environment of Pb by Fe ions in the PFB0 configuration produces the largest moment.

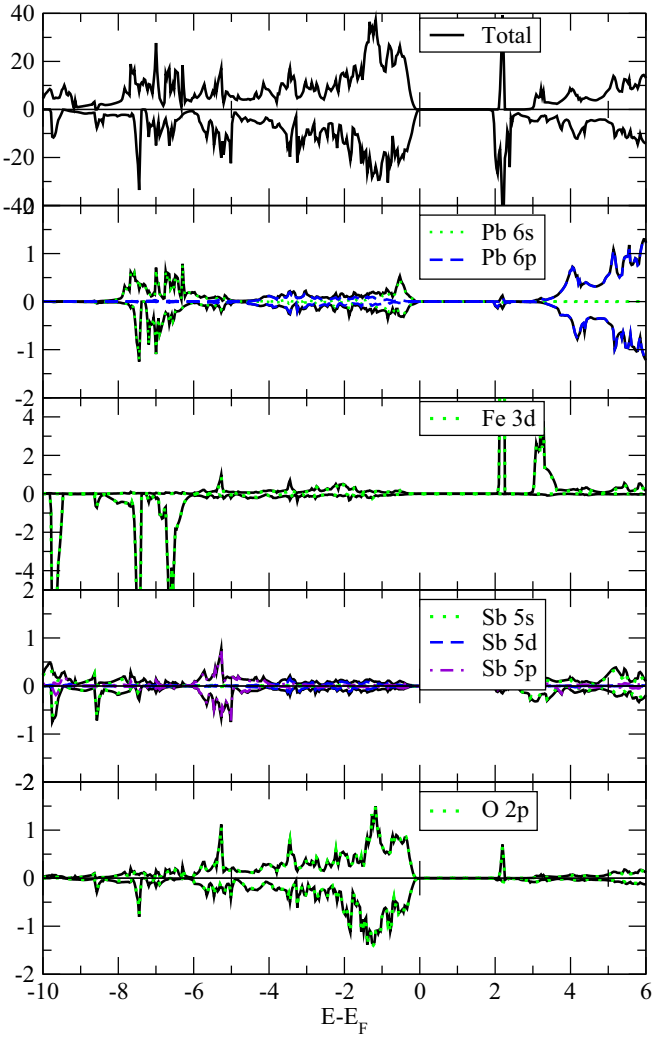

FIG. 12. Spin-resolved total DOS (top panel) for the PFB0 configuration, $U = 6$ eV. Other panels show selected densities of states projected onto the basis functions (green, blue, and magenta lines), which maximally contribute to the total DOS near the Fermi level. Solid black lines represent total DOS contributions of individual ion species.

The moment for the PFB5 configuration is more than two times smaller, whereas for the PFB2 configuration it is 25% smaller than in the PFB0 case. Therefore, in the samples with high degree of disorder, a prevailing number of Pb ions are found in nontetrahedral environment, with a small hyperfine field at the nuclei. This may explain the emergence of the second broad resonance peak in disordered samples, at a frequency below the one exhibited by ordered samples of the PFB0 configuration.

Figure 12 displays the total and projected densities of states (DOS) for the ordered configuration PFB0. It is straightforward to observe that the states near the Fermi level are formed by Pb 6*s* and 6*p*, Fe 3*d*, and O 2*p* orbitals. Sb ions are almost ionized, only Sb 5*p* orbitals give a small contribution to the valence band at energies $-6\,\mathrm{eV} < E - E_{\mathrm{F}} < -5\,\mathrm{eV}$.

Qualitatively identical pictures of calculated DOS are observed for PFB5 and PFB2 configurations. For example, Fig. 13 shows DOS for the layered PFB5 configuration. On the other hand, one can recognize drastic changes in the valence band

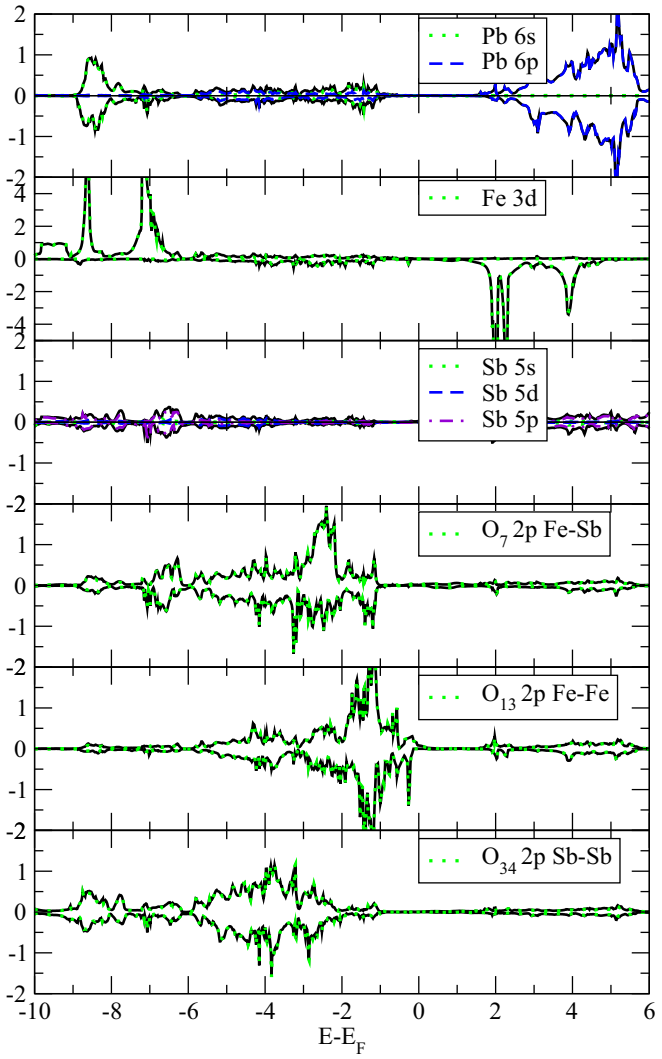

FIG. 13. Same as in Fig. 12 for the PFB5 configuration. Oxygen p states are calculated for all three nonequivalent configurations: Fe-O_{13}-Fe, Fe-O_7-Sb, and Sb-O_{34}-Sb.

due to a rather different behavior of oxygen p states. Oxygen ions have three nonequivalent positions in this configuration, Fe-O_{13}-Fe, Fe-O_7-Sb, and Sb-O_{34}-Sb, respectively (see Fig. 2). These three arrangements participate in the chemical bonding in considerably different ways. The top of the valence band is formed by the 2p states of oxygen ions situated between two Fe ions, whereas all states of the other ions are lowered by 1 eV (see Sec. IV B below for more details).

B. Pb 6*s*-Fe 3*d* hybridization

DFT calculations reveal strong hybridization between Pb 6s and O 2p orbitals. By analyzing the O 2p and Pb 6s LDOS calculations [carried out for PFB0, Fig. 14(a)], one can recognize that hybridization takes place both at the top and near the bottom of the valence band and it is responsible for the appearance of Pb 6s density just below the Fermi level. In accordance with Refs. [46,47], this hybridization stimulates the formation of bonding-antibonding orbitals and leads to the emergence of lobes in distorted compounds due to partial localization of Pb 6s electron density on antibonding Pb-O orbitals. In lead, containing perovskites, the formation of such lobes contributes to ferroelectric (FE) distortion and can compensate, to a certain extent, for the suppression of FE distortion caused by incorporation of magnetic ions with a partially filled d shell.

Being located under the Fermi level, both Pb 6s and O 2p bonding-antibonding orbitals are completely filled. Such hybridization by itself does not contribute to the decrease or increase of the total energy. Involvement of partially filled orbitals is thus necessary for the formation of chemical bond. In the case of PFB0, the hybridization between Pb 6s and O 2p orbitals occurs with some participation of Fe 3d states and results in a hybridization of Pb 6s and Fe 3d orbitals [Fig. 14(b)]. This leads to a polarization of Pb 6s states due to the different occupation of the Pb 6s orbitals with spin "up" and spin "down" (Table II). As the spin density is nonzero at the site of the nucleus, it results in the emergence of a superhyperfine field at the Pb site.

Taking into account that polarization transfer occurs through oxygen atoms, it is necessary to distinguish the ways the hybridization takes place for different types of oxygen. In contrast to the ordered PFB0 configuration, where all the oxygen atoms are equivalent and are positioned between Fe and Sb atoms, PFB5 and PFB2 chemical configurations have three nonequivalent oxygen atoms belonging to Sb-O-Fe, Fe-O-Fe, and Sb-O-Sb environments (respectively O_7, O_{13}, and O_{34} in Figs. 2 and 13). According to the calculations performed for PFB5 and PFB2 chemical configurations, all three types of oxygen hybridize in a substantially different manner (Fig. 13). It can be seen that the oxygen atoms, located between two Sb atoms, exhibit a much stronger hybridization of their 2p orbitals with Pb 6s ones (near the bottom of the valence band) than those located between Sb and Fe atoms. At the same time, this hybridization almost vanishes for oxygen atoms located in the iron-only environment. In addition, all oxygen 2p energy levels in PFB2 and PFB5 configurations are shifted with respect to each other for different types of oxygen (Fig. 13). The oxygen ions in the Fe-O-Fe environment have the lowest energies of their 2p orbitals. Their energy gradually increases on substituting one or two atoms of Fe by Sb. This can be explained in terms of the substantially different charge states of the Fe^{+3} and Sb^{+5} ions in these compounds. A substantially higher positive charge of the Sb ions thus leads to formation of Sb-O orbitals with higher (than Fe-O orbitals) binding energy. Due to the relatively high binding energy of the Pb 6s orbitals (about 8 eV), it is more favorable for them to hybridize with the oxygen ions having more deep-seated orbitals, as in the case of oxygen in the Sb-O-Sb environment. On the other hand, the Pb 6s LDOS for the PFB2 configuration is noticeably shifted towards lower energies, as compared to ordered PFB0 (Fig. 15). This evidences the energy benefit for Pb to form a chemical bond with oxygen ions with no iron in their nearest surrounding. Consequently, the magnetic field transferred from Fe^{3+} ions to Pb nucleus is much lower in disordered samples.

It is worth noting that, despite the fact that our calculations do not show pronounced hybridization between Pb 6s and 6p orbitals, their hybridization may partially contribute to the participation of Pb 6s electrons in the chemical bonding. In the case of ordered compounds, Fe^{3+} ions form a regular

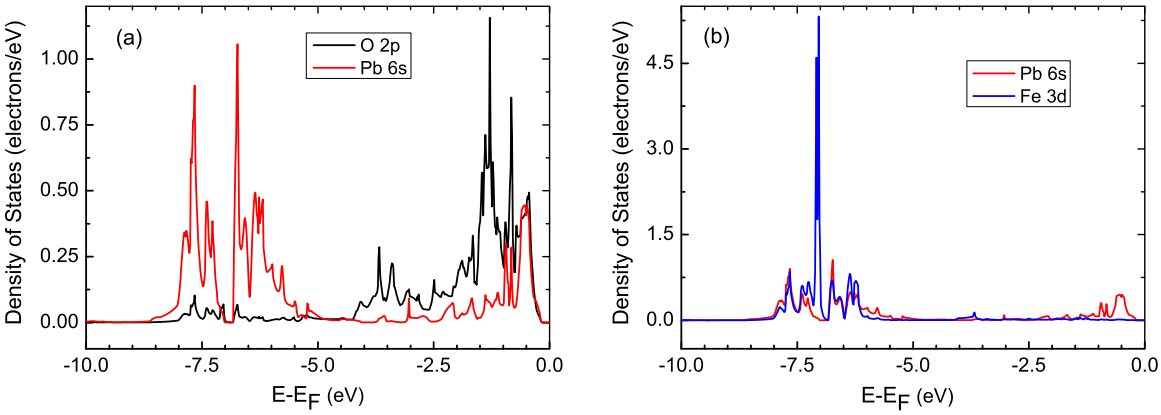

FIG. 14. (a) O 2*p*, Pb 6*s* LDOS and (b) Pb 6*s*, Fe 3*d* LDOS for the PFB0 chemical configuration.

tetrahedron around Pb ions. This could contribute to the formation of hybridized Pb 6*s* p^3 orbitals pointing towards the corners of the tetrahedron, and thus in turn play an additional role in the polarization of Pb 6*s* orbitals via Fe^{3+} ions.

V. CONCLUSIONS

In conclusion, we performed measurements of magnetic susceptibility, Fe^{3+} EPR and ^{207}Pb NMR spectra in the magnetoelectric multiferroic $Pb(Fe_{1/2}Sb_{1/2})O_3$, synthesized at high hydrostatic pressure (6 GPa) and temperature in the 1200 K–1800 K range. By varying the temperature and duration time of the synthesis, we were able to fabricate ceramic samples with different degrees of chemical ordering of the Fe^{3+} and Sb^{5+} ions over the octahedral positions. The effective ordering degree parameter $s_{\rm eff}$ determined from the XRD data, varies from 0.21 to 0.93. Using a similar approach, ceramic samples of xPb$(Fe_{1/2}Sb_{1/2})O_3$−(1-x) Pb$(Fe_{1/2}Nb_{1/2})O_3$ solid solutions were also fabricated and studied by ^{207}Pb NMR. By combining XRD and NMR data, we calculated the long-range order parameter s and the volume fraction of the ordered regions s'.

Magnetic measurements of PFS ceramics with high degree of chemical order ($s_{\rm eff} = 0.93$) reveal a distinct magnetic susceptibility anomaly at the Neel temperature of 32 K, as well as a broad bump between 100–150 K, arising from collective freezing of superparamagnetic clusters created in disordered PFS regions at around 250 K. In the samples with substantial chemical disorder ($s_{\rm eff} = 0.21-0.46$), the low-temperature susceptibility maximum shifts to 20 K. Moreover, ZFC and FC curves do not match at $T < 20$ K, demonstrating the onset of the spin glass state. The anomaly at 100–150 K gradually disappears as the chemical disorder increases. At the same time, local-probe EPR measurements of the most disordered sample ($s_{\rm eff} = 0.21$) suggest that small thermally reorientable AFM clusters are created already at 40–50 K. This differs from the behavior of disordered PFN or PFT where long-range AFM spin order appears at $T < T_{\rm N} \approx 150$ K [41,48,49].

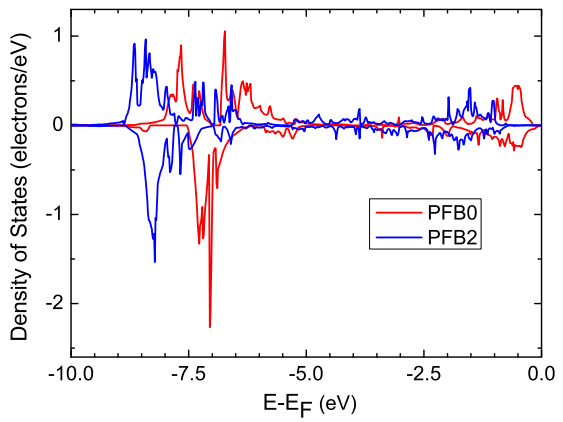

FIG. 15. Pb 6*s* LDOS for PFB0 and PFB2 chemical configurations.

In order to explain the difference between the magnetic properties of disordered PFS and PFN, we measured ^{207}Pb NMR spectra in PFS samples with different chemical order and in xPFS − (1-x)PFN solid solutions. PFS spectra consist of two spectral lines, originating from chemically ordered and disordered regions, demonstrating heterogeneous ordering, with ordered (or partially ordered) regions embedded in the disordered matrix. A similar two-component spectrum is observed in the xPFS − (1-x)PFN solid solutions. Here, the perfect order, existing at $x = 1$, is nearly destroyed at a PFN concentration of only 50%−60%. Only a single spectral line is detected in the spectrum for $x < 0.4$, demonstrating that the solid solution is completely disordered. In our opinion, the difference in the magnetic properties of PFN and PFS is related to the fact that PFN (as well as PFT) is a completely disordered material (the long-range order parameter $s = 0$), whereas PFS is only heterogeneously disordered, with small ordered regions preventing the percolation of the nearest-neighbor Fe-Fe interaction across the lattice. Strong nearest-neighbor Fe-Fe interactions, responsible for the appearance of AFM phase in PFN at $T_{\rm N} \approx 150$ K, are thus inhibited in heterogeneously disordered PFS. Consequently, only a short-ranged spin order is present in disordered PFS.

^{207}Pb NMR spectra, measured in PFS samples with different ordering degrees of Fe and Sb ions as well as in xPFS − (1-x)PFN solid solutions, reveal direct correlation between the paramagnetic shift of ^{207}Pb NMR line and the degree of its chemical ordering. We attribute this to the existence of an extremely high Fermi-contact superhyperfine magnetic field at the Pb nuclear site ($H_{\rm hf} = 8$ kOe) in the regions

with 1:1 ordering of Fe^{3+} and Sb^{5+} ions as compared to areas where such ordering does not exist. We also observe that the superhyperfine field, arising from the Fermi contact interaction, is almost zero in PFN, which is a completely disordered material.

Theoretical calculations, performed for the ordered and various disordered PFS configurations, reveal a noticeably higher hybridization between Pb 6*s* and Fe 3*d* orbitals in the ordered configuration. This hybridization leads to the polarization of the Pb 6*s* states by the magnetic moment of Fe^{3+} ions and results in the appearance of a superhyperfine field at Pb sites. According to our theoretical calculations, Pb 6*s*–Fe 3*d* hybridization is mediated by O 2*p* states. It strongly depends on the chemical order, due to the existence of three different types of oxygen environments in disordered configurations, resulting in a preferential formation of the chemical bond between Pb 6*s* orbitals and oxygen ions located between two antimony ions. The absence of such arrangement in the highly-ordered compounds gives rise to an unusually high superhyperfine field at the Pb site.

Let us finally emphasize the special role of Pb ions, both in the enhancement of superparamagnetism and in the creation of the ferroelectric phase in PFS. This statement is supported by the fact that a similar material, chemically ordered lead-free $Sr(Fe_{1/2}Sb_{1/2})O_3$, exhibits neither ferroelectric nor superparamagnetic or magnetoelectric properties [50]. The strong superparamagnetism, emerging from the formation of Fe^{3+} spin clusters with a giant total magnetic moment, may also result in a strong paramagnetoelectric effect in PFS. Recently, such behavior has been reported for a cluster-glass magnetic phase in a PFN–$PbTiO_3$ solid solution [6]. This phenomenon, however, needs further investigation.

ACKNOWLEDGMENTS

We gratefully acknowledge the support of Czech Science Foundation (Grant No. 13–11473S), Operational Program "Research and Development for Innovation" of the Czech Republic (Grant No. CZ.1.05/4.1.00/16.0340), NATO (Belgium) (Grant No. SfP-984735), Belarusian Republican Foundation for Fundamental Research (Grant No. T16R-079), Russian Foundation for Basic Research (Grant No. 16-52-00072 Bel_a), and Ministry of Education and Science of the Russian Federation (research Project No. 3.1649.2017/4.6). R.O.K. and I.V.K. thank M. D. Kuz'min and K. Koepernik for very useful discussions, U. Nitzsche and A. Lihtin for technical assistance, and IFW Dresden (Germany) for the use of their computer facilities.

[1] N. Ortega, A. Kumar, J. F. Scott, and R. S. Katiyar, Multifunctional magnetoelectric materials for device applications, J. Phys.: Condens. Matter **27**, 504002 (2015)

[2] A. P. Pyatakov and A. K. Zvezdin, Magnetoelectric and multiferroic media, Phys. Usp. **55**, 557 (2012).

[3] T. Zhao, A. Scholl, F. Zavaliche, K. Lee, M. Barry, A. Doran, M. P. Cruz, Y. H. Chu, C. Ederer, N. A. Spaldin, R. R. Das, D. M. Kim, S. H. Baek, C. B. Eom, and R. Ramesh, Electrical control of antiferromagnetic domains in multiferroic $BiFeO_3$ films at room temperature, Nat. Mater. **5**, 823 (2006).

[4] S. H. Chun *et al.*, Electric Field Control of Nonvolatile Four-State Magnetization at Room Temperature, Phys. Rev. Lett. **108**, 177201 (2012).

[5] V. V. Laguta, A. N. Morozovska, E. I. Eliseev, I. P. Raevski, S. I. Raevskaya, E. I. Sitalo, S. A. Prosandeev, and L. Bellaiche, Room-temperature paramagnetoelectric effect in magnetoelectric multiferroics $Pb(Fe_{1/2}Nb_{1/2})O_3$ and its solid solution with $PbTiO_3$, J. Mater. Sci. **51**, 5330 (2016).

[6] V. V. Laguta, V.A. Stephanovich, I. P. Raevski, S. I. Raevskaya, V. V. Titov, V. G. Smotrakov, and V. V. Eremkin Magnetoelectric effect in antiferromagnetic multiferroic $Pb(Fe_{1/2}Nb_{1/2})O_3$ and its solid solutions with $PbTiO_3$, Phys. Rev. B **95**, 014207 (2017).

[7] D. A. Sanchez, N. Ortega, A. Kumar, R. Roque-Malherbe, R. Polanco, J. F. Scott, and R. S. Katiyar, Symmetries and multiferroic properties of novel room-temperature magnetoelectrics: Lead iron tantalate–lead zirconate titanate (PFT/PZT), AIP Advances **1**, 042169 (2011).

[8] D. Evans, A. Schilling, A. Kumar, D. Sanchez, N. Ortega, M. Arredondo, R. Katiyar, J. Gregg, and J. Scott, Magnetic switching of ferroelectric domains at room temperature in multiferroic PZTFT, Nat. Commun. **4**, 1534 (2013).

[9] D. A. Sanchez, N. Ortega, A. Kumar, G. Sreenivasulu, R. S. Katiyar, J. F. Scott, D. M. Evans, M. Arredondo-Arechavala, A. Schilling, and J. M. Gregg, Room-temperature single phase multiferroic magnetoelectrics: $Pb(Fe,M)_x(Zr,Ti)_{(1-x)}O_3$ [M = Ta, Nb], J. Appl. Phys. **113**, 074105 (2013).

[10] M. A. Carpenter *et al.*, Elastic and magnetoelastic relaxation behaviour of multiferroic (ferromagnetic +ferroelectric + ferroelastic) $Pb(Fe_{0.5}Nb_{0.5})O_3$ perovskite, J. Phys.: Condens. Matter **27**, 285901 (2015).

[11] B. Fraygola, A. A. Coelho, and J. A. Eiras, Magnetic and electric ordering and intrinsic magnetoelectric coupling in $Pb(Fe,W)O_3$ based ceramics, Ferroelectrics **442**, 50 (2013).

[12] D. D. Khalyavin, A. N. Salak, N. M. Olekhnovich, A. V. Pushkarev, Yu. V. Radyush, P. Manuel, I. P. Raevski, M. L. Zheludkevich, and M. G. S. Ferreira, Polar and antipolar polymorphs of metastable perovskite $BiFe_{0.5}Sc_{0.5}O_3$, Phys. Rev. B **89**, 174414 (2014).

[13] V. V. Laguta, V. A. Stephanovich, M. Savinov, M. Marysko, R. O. Kuzian, I. V. Kondakova, N. M. Olekhnovich, A. V. Pushkarev, Yu. V. Radyush, I. P. Raevski, S. I. Raevskaya, and S. A. Prosandeev, Superspin glass phase and hierarchy of interactions in multiferroic $PbFe_{1/2}Sb_{1/2}O_3$: An analog of ferroelectric relaxors? New J. Phys. **16**, 113041 (2014).

[14] S. V. Misjul, M. S. Molokeev, N. M. Olekhnovich, A. V. Pushkarev, J. V. Radyush, I. P. Raevski, and I. N. Safonov, Synthesis and Crystal Structure of the Ordered Perovskite Pb_2FeSbO_6, J. Siberian Federal Univ. Math. Phys. **6**, 227 (2013).

[15] I. P. Raevski, S. P. Kubrin, S. I. Raevskaya, D. A. Sarychev, S. A. Prosandeev, and M. A. Malitskaya, Magnetic properties of $PbFe_{1/2}Nb_{1/2}O_3$: Mossbauer spectroscopy and first-principles calculations, Phys. Rev. B **85**, 224412 (2012).

[16] R. O. Kuzian, I. V. Kondakova, A. M. Daré, and V. V. Laguta, Magnetic interactions in disordered perovskite $PbFe_{1/2}Nb_{1/2}O_3$ and related compounds: Dominance of nearest-neighbor interaction, Phys. Rev. B **89**, 024402 (2014).

[17] R. O. Kuzian, V. V. Laguta, and J. Richter, Lieb-Mattis ferrimagnetic superstructure and superparamagnetism in Fe-based double perovskite multiferroics, Phys. Rev. B **90**, 134415 (2014).

[18] N. Lampis, C. Franchini, G. Satta, A. Geddo-Lehmann, and S. Massidda, Electronic structure of $PbFe_{1/2}Ta_{1/2}O_3$: Crystallographic ordering and magnetic properties, Phys. Rev. B **69**, 064412 (2004).

[19] I. P. Raevski, S. P. Kubrin, S. I. Raevskaya, V. V. Stashenko, D. A. Sarychev, M. A. Malitskaya, M. A. Seredkina, V. G. Smotrakov, I. N. Zakharchenko, and V. V. Eremkin, Dielectric and Mossbauer studies of perovskite multiferroics, Ferroelectrics **373**, 121 (2008).

[20] A. A. Gusev *et al.*, Electron microscopy, X-ray diffraction and Mossbauer studies of $PbFe_{0.5}Nb_{0.5}O_3$, $PbFe_{0.5}Ta_{0.5}O_3$ and $BaFe_{0.5}Nb_{0.5}O_3$ ceramics sintered from mechanoactivated nanopowders, Ferroelectrics **496**, 231 (2016).

[21] S. A. Prosandeev, I. P. Raevski, S. I. Raevskaya, and H. Chen, Influence of epitaxial strain on clustering of iron in $Pb(Fe_{1/2}Nb_{1/2})O_3$ thin films, Phys. Rev. B **92**, 220419(R) (2015).

[22] I. P. Raevski *et al.*, Structural, dielectric and Mossbauer studies of $PbFe_{0.5}Sb_{0.5}O_3$ ceramics with differing degree of compositional ordering, Ferroelectrics **501**, 154 (2016).

[23] N. Setter and L. E. Cross, The contribution of structural disorder to diffuse phase transitions in ferroelectrics, J. Mater. Sci. **15**, 2478 (1980).

[24] C. G. F. Stenger and A. J. Burggraaf, Order–disorder reactions in the ferroelectric perovskites $Pb(Sc_{1/2}Nb_{1/2})O_3$ and $Pb(Sc_{1/2}Ta_{1/2})O_3$. II. Relation between ordering and properties, Phys. Status Solidi A **61**, 275 (1980).

[25] A. A.Bokov and I. P. Rayevsky Compositional ordering in ferroelectrics with diffuse phase transition, Ferroelectrics **90**, 125 (1989).

[26] I. P. Raevski, V. Yu. Shonov, M. A. Malitskaya, E. S. Gagarina, V. G. Smotrakov, and V. V. Eremkin, X-ray and dielectric studies of liquid-phase sintered $PbB^{3+}_{1/2}B^{5+}_{1/2}O_3$ ceramics with differing degree of compositional ordering, Ferroelectrics **235**, 205 (1999).

[27] I. P. Raevski *et al.*, Random-site cation ordering and dielectric properties of $PbMg_{1/3}Nb_{2/3}O_3$-$PbSc_{1/2}Nb_{1/2}O_3$, Integrated Ferroelectrics **53**, 475 (2003).

[28] R. W. Schurko, I. Hung, and C. M. Widdifield, Signal enhancement in NMR spectra of half-integer quadrupolar nuclei via DFS- QCPMG and RAPT–QCPMG pulse sequences, Chem. Phys. Lett. **379**, 1 (2003).

[29] R. Ernst, S. Bodenhausen, and A. Wokaun, in *Principles of NMR in One and Two Dimensions* (Oxford University Press, New York, 1987).

[30] S. Bedanta and W. Kleemann, Supermagnetism, J. Phys. D: Appl. Phys. **42**, 013001 (2009).

[31] J. A. Mydosh, *Spin Glasses: An Experimental Introduction* (Taylor and Francis, London, 1993).

[32] R. M. White, *Quantum Theory of Magnetism* (Springer-Verlag, Berlin, Heidelberg, New York, 1983).

[33] A. Lohmann, H.-J. Schmidt, and J. Richter, Tenth-order high temperature expansion for the susceptibility and the specific heat of spin-s Heisenberg models with arbitrary exchange patterns: Application to pyrochlore and kagome magnets, Phys. Rev. B **89**, 014415 (2014).

[34] M. Maryško, V. V. Laguta, I. P. Raevski, R. O. Kuzian, N. M. Olekhnovich, A. V. Pushkarev, Yu. V. Radyush, S. I. Raevskaya, V. V. Titov and S. P. Kubrin, Magnetic susceptibility of multiferroics and chemical ordering, AIP Adv. **7**, 056409 (2017)

[35] B. C. Tofield and B. E. F. Fender, Covalency parameters for Cr^{3+}, Fe^{3+}, and Mn^{4+} in an oxide environment, J. Phys. Chem. Solids **31**, 2741 (1970).

[36] W. Kleemann, V. V. Shvartsman, P. Borisov, and A. Kania, Coexistence of Antifwerromagnetic and Spin Cluster Glass Order in the Magnetoelectric Relaxor Multiferroic $PbFe_{0.5}Nb_{0.5}O_3$, Phys. Rev. Lett. **105**, 257202 (2010).

[37] V. V. Laguta, J. Rosa, L. Jastrabik, R. Blinc, P. Cevc, B. Zalar, M. Remskar, S. I. Raevskaya, and I. P. Raevski, ^{93}Nb NMR and Fe^{3+} EPR study of local magnetic properties of magnetoelectric $Pb(Fe_{1/2}Nb_{1/2})O_3$, Mater. Res. Bull. **45**, 1720 (2010).

[38] A. Abragam, *The Principles of Nuclear Magnetism* (Oxford University Press, Oxford, 1961).

[39] M. B. Walker, Exchange interactions from nuclear magnetic resonance linewidths, Proc. Phys. Soc. **87**, 45 (1966).

[40] T. Moriya, Nuclear magnetic relaxation in antiferromagnetics, II. Progr, Theor. Phys. **16**, 641 (1956).

[41] S. A. Ivanov, R. Tellgren, H. Rundlof, N. W. Thomas, and S. Ananta, Investigation of the structure of the relaxor ferroelectric $Pb(Fe_{1/2}Nb_{1/2})O_3$ by neutron powder diffraction, J. Phys.: Condens. Matter **12**, 2393 (2000).

[42] V. A. Stephanovich and V. V. Laguta, Transversal spin freezing and re-entrant apin glass phases in chemically disordered Fe-containing perovskite multiferroics, Phys. Chem. Chem. Phys. **18**, 7229 (2016).

[43] H. Eschrig, K. Koepernik, and I. Chaplygin, Density Functional Application to Strongly Correlated Electron Systems, J. Solid State Chem. **176**, 482 (2003).

[44] M. T. Czyzyk and G. A. Sawatzky, Local-density functional and on-site correlations: The electronic structure of La_2CuO_4 and $LaCuO_3$, Phys. Rev. B **49**, 14211 (1994).

[45] Computer code FPLO-9.00-34 [improved version of the original FPLO code by K. Koepernik and H. Eschrig, Full-potential nonorthogonal local-orbital minimum-basis band-structure scheme, Phys. Rev. B **59**, 1743 (1999)]; http://www.FPLO.de.

[46] G. W. Watson and S. C. Parker, Origin of the Lone Pair of α-PbO from Density Functional Theory Calculations, J. Phys. Chem. B **103**, 1258 (1999).

[47] G. W. Watson, S. C. Parker, and G. Kresse, *Ab initio* calculation of the origin of the distortion of a-PbO, Phys. Rev. B **59**, 8481 (1999).

[48] S. A. Ivanov, S. Eriksson, N. W. Thomas, R. Tellgren, and H. Rundlof, A neutron powder diffraction study of the ferroelectric relaxor $Pb(Fe_{1/2}Ta_{1/2})O_3$, J. Phys.: Condens. Matter **13**, 25 (2001).

[49] V. V. Laguta, M. D. Glinchuk, M. Maryško, R. O. Kuzian, S. A. Prosandeev, S. I. Raevskaya, V. G. Smotrakov, V. V. Eremkin, and I. P. Raevski, Effect of Ba and Ti doping on magnetic properties of multiferroic $Pb(Fe_{1/2}Nb_{1/2})O_3$, Phys Rev B **87**, 064403 (2013).

[50] E. J. Cussen, J. F. Vente, P. D. Battle, and T. C. Gibb, Neutron diffraction study of the influence of structural disorder on the magnetic properties of Sr_2FeMO_6 (M = Ta, Sb), J. Mater. Chem. **7**, 459 (1997).